

Covariance-Guided DFT Beam Selection for Beamspace ESPRIT in Hybrid mmWave MIMO Receivers

Rıfat Volkan Şenyuva

Department of Electrical–Electronics Engineering,
Maltepe University, Istanbul 34857, Turkey
rifatvolkansenyuva@maltepe.edu.tr

30.11.2025

Abstract

We consider direction-of-arrival estimation in hybrid analog/digital mmWave MIMO receivers that employ DFT beamspace processing with a limited number of RF chains. Building on beamspace ESPRIT, we develop a covariance-guided beam selection framework that reconstructs a virtual fully digital subarray, fits a structured signal-plus-noise covariance model, and uses the resulting denoised covariance to select, for each coarse sector, a small contiguous block of DFT beams under a beam-budget constraint. The selected beams feed a sparse beamspace Unitary ESPRIT stage, so that the overall complexity is dominated by a single low-dimensional ESPRIT call while retaining a large effective aperture. Monte Carlo simulations for a 32-element uniform linear array with three paths show that, relative to a standard sectorization-based beam selector built on the same DFT codebook and ESPRIT estimator, the proposed method attains near Cramér–Rao bound accuracy at moderate array signal-to-noise ratios, substantially reduces the gap to the bound and the failure rate, and offers favorable accuracy–runtime trade-offs under dynamic RF budgets and sector-edge stress tests.

Keywords: DoA estimation, hybrid mmWave MIMO, DFT beamspace, covariance-guided beam selection, beamspace ESPRIT, Unitary ESPRIT, array signal processing

1 Introduction

We consider direction-of-arrival (DoA) estimation in hybrid analog/digital (HAD) mmWave multiple-input multiple-output (MIMO) receivers that employ discrete Fourier transform (DFT) beamspace processing with a limited number of radio-frequency (RF) chains. In such architectures, only a few linear combinations of antenna outputs are observed in each training slot, which makes it challenging to achieve high-resolution spatial frequency estimation over a practical range of array signal-to-noise ratios (ASNRs). Our goal is to design a two-stage estimator that attains near-Cramér–Rao bound (CRB) performance while respecting strict constraints on RF chain count and beam budget.

The problem is motivated by ongoing work toward beyond-5G and 6G systems, where extremely wide bandwidths, high carrier frequencies, and large-scale antenna arrays are expected to coexist with stringent power and hardware constraints [1–3]. Recent studies on near-field wideband channel estimation for extremely large-scale MIMO further highlight the need for accurate yet efficient spatial inference when arrays scale to hundreds or thousands of effective antenna dimensions [4, 5]. In this context, HAD architectures and beamspace processing are attractive because they reduce RF chain count while maintaining large apertures.

Within this broader context, DoA estimation in HAD receivers has received renewed attention. One line of work adapts classical subspace and maximum-likelihood methods to hybrid

front-ends, addressing ambiguity and latency issues by carefully designing training sequences and analog combiners [6, 7]. Other works exploit learning-based modules to improve robustness, for example by modeling the distribution of DoA errors, designing robust analog/digital beamformers, or jointly handling sensing and communication tasks in integrated systems [8–10]. A complementary line focuses on covariance reconstruction from beam-swept measurements, which enables the use of element-space algorithms at the cost of additional training overhead and matrix inversion steps [11].

Sparse and gridless DoA estimation methods provide another powerful set of tools. Sparse reconstruction and compressed sensing techniques, as surveyed in [12], motivated on-grid formulations that approximate the angular domain by a discrete grid. More recent contributions have developed off-grid or gridless variants that avoid basis mismatch by exploiting structured covariance models, Bayesian priors, or atomic norm formulations [13–17]. These approaches can approach the CRB and handle coherent sources, but they are typically formulated in element space, often involve semidefinite programming or other heavy optimization, and are not tailored to beam selection for DFT beamspace ESPRIT.

Beamspace ESPRIT provides a complementary perspective that exploits both array structure and hybrid implementation. Tensor-ESPRIT and related frameworks in DFT beamspace use two-stage hybrid training protocols: a coarse DoA estimation phase on a reduced array, followed by sectorization of the angular domain and a high-resolution Tensor-ESPRIT step in carefully chosen DFT beams [18]. Recent analytical work has derived first-order mean-squared-error (MSE) expressions for 1-D ESPRIT in DFT beamspace, compared them with element-space ESPRIT, and studied the impact of effective aperture and beam patterns on performance [19, 20]. Beamspace ESPRIT has also been analyzed in a non-asymptotic framework, yielding deterministic bounds and informing the design of multi-resolution analog beamformers via max–min criteria on beamforming gain [21]. These results show that beamspace processing can be both hardware-efficient and statistically attractive when the selected beams are well matched to the dominant paths and when the effective aperture is preserved.

Despite these advances, existing hybrid channel-estimation and beamspace ESPRIT frameworks typically rely on sectorization or beam-sweeping schemes that are only loosely coupled to the observed data. Sliding-window sectorization determines sectors using coarse DoA estimates and then activates pre-defined contiguous beam groups inside each sector [18]. Beam-sweeping covariance reconstruction, in contrast, requires potentially many training beams to invert a linear system and is tailored to element-space MUSIC rather than to DFT beamspace ESPRIT [11]. In both cases, three limitations arise. First, the sample covariance structure is only partially exploited, for example through coarse point estimates or power measurements, even though it encodes the signal subspace and path powers. Second, to remain robust against coarse-estimation errors and sector-edge effects, sectorization and sweeping schemes often activate more beams than strictly necessary, which increases training overhead and the computational burden of the fine-stage estimator. Third, most existing designs do not quantify or directly control how beam patterns, beam counts, and aperture reduction affect ESPRIT accuracy under RF-chain and beam-budget constraints.

In this paper, we develop a covariance-guided beam selection framework for the DFT beamspace ESPRIT in hybrid mmWave MIMO receivers. Starting from measurements collected on a centro-symmetric element-space subarray during a short hybrid training phase, we reconstruct a virtual full-aperture signal-plus-noise covariance matrix by solving a low-rank Toeplitz positive-semidefinite covariance-fitting problem. The reconstructed covariance serves as a denoised proxy for the array response. For each candidate contiguous subset of DFT beams inside a sector, we then compute a simple score that reflects both captured signal energy and effective aperture, motivated by analytical MSE expressions for beamspace ESPRIT. Under an explicit beam-budget constraint, we select, for each sector, the best contiguous block of beams according to this score and apply a sparse beamspace Unitary ESPRIT estimator to the re-

sulting reduced-dimensional sector of interest. The overall complexity is dominated by a single low-dimensional ESPRIT call, while the covariance-guided beams allow the estimator to operate near the CRB in many scenarios.

Our contributions can be summarized as follows:

- We introduce a covariance-guided DFT beam selection scheme for hybrid mmWave MIMO receivers. Using measurements from an element-space subarray, we fit a Toeplitz-structured signal-plus-noise covariance model and reconstruct a denoised full-aperture signal covariance, which we then use to score and select contiguous DFT beam subsets inside pre-defined sectors under an explicit beam-budget constraint.
- We design a simple beam scoring rule and selection algorithm that incorporate insights from analytical MSE expressions and error bounds for ESPRIT in DFT beamspace [19, 21]. The resulting beam sets concentrate signal energy around the dominant paths, preserve a large effective aperture, and satisfy the shift-invariance and contiguity requirements of beamspace Unitary ESPRIT.
- We integrate the covariance-guided selector into a two-stage hybrid training and estimation framework and benchmark it against a sectorization-based baseline that relies on fixed beam groups derived from coarse estimates. Through Monte Carlo simulations, we compare the methods in terms of root-mean-squared error (RMSE), gap to the CRB, failure rate, and runtime under varying ASNRs, snapshot numbers, beam budgets, and sector-edge conditions, and we show that the proposed method achieves a favorable accuracy–complexity trade-off.

The rest of the paper is organized as follows. Section 2 introduces the system and data model and the hybrid training protocol. Section 3 presents the proposed covariance-guided beam selection framework, including the covariance-fitting formulation and the sparse beamspace Unitary ESPRIT estimator. Section 4 contains numerical experiments that illustrate the performance and complexity trade-offs of the proposed method in several representative scenarios. Section 5 concludes the paper and outlines directions for future work.

2 System Model

In this section we specify the array data model, the hybrid beamforming architecture, and the resulting beamspace signal model that will be used throughout the paper.

2.1 Signal Model at the Array Elements

We consider a ULA composed of M antennas receiving signals from d uncorrelated, far-field, narrow-band sources. The spatial frequencies of the sources are collected in the vector

$$\boldsymbol{\mu} \triangleq [\mu_1, \dots, \mu_d]^T,$$

where μ_k is related to the physical angle-of-arrival θ_k via $\mu_k = -\pi \sin(\theta_k)$. Let $\mathbf{a}(\mu_k) \in \mathbb{C}^M$ denote the corresponding steering vector,

$$\mathbf{a}(\mu_k) \triangleq [1, e^{j\mu_k}, \dots, e^{j(M-1)\mu_k}]^T,$$

and define the array manifold matrix

$$\mathbf{A}(\boldsymbol{\mu}) \triangleq [\mathbf{a}(\mu_1), \dots, \mathbf{a}(\mu_d)] \in \mathbb{C}^{M \times d}.$$

We collect N_{snap} snapshots at the array output in the matrix $\mathbf{Y} \in \mathbb{C}^{M \times N_{\text{snap}}}$, modeled as

$$\mathbf{Y} = \mathbf{A}(\boldsymbol{\mu})\mathbf{S} + \mathbf{N} \tag{1}$$

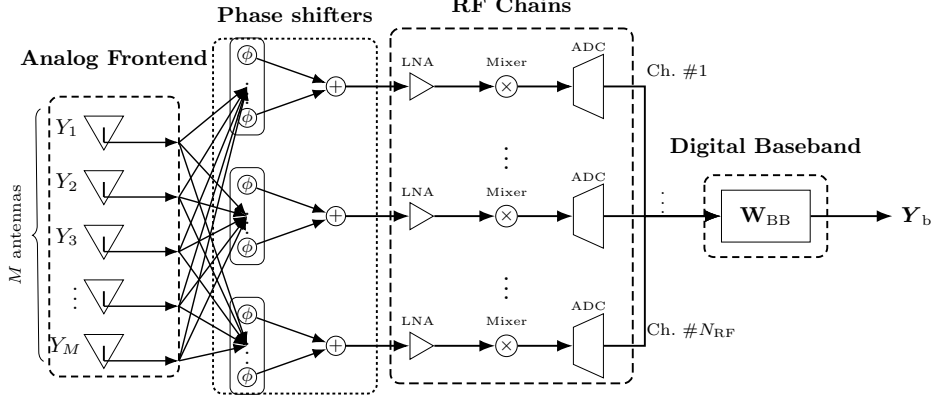


Figure 1: Hybrid MIMO receiver with M antennas and N_{RF} RF chains. The analog combiner \mathbf{W}_{RF} is implemented by a fully-connected phase-shifter network, and the digital combiner \mathbf{W}_{BB} operates at baseband.

where the n -th column of $\mathbf{S} \in \mathbb{C}^{d \times N_{\text{snap}}}$ contains the source symbols at snapshot n , and the n -th column of $\mathbf{N} \in \mathbb{C}^{M \times N_{\text{snap}}}$ contains additive noise samples. We assume that the source symbols are zero-mean, mutually uncorrelated, and temporally white, with covariance

$$\mathbf{R}_s \triangleq \mathbb{E}\{\mathbf{s}[n]\mathbf{s}^H[n]\} = \text{diag}(p_1, \dots, p_d),$$

and that the noise is spatially and temporally white,

$$\mathbf{n}[n] \sim \mathcal{CN}(\mathbf{0}_M, N_0 \mathbf{I}_M), \quad n = 1, \dots, N_{\text{snap}}.$$

The theoretical array covariance is then

$$\mathbf{R}_y \triangleq \mathbb{E}\{\mathbf{y}[n]\mathbf{y}^H[n]\} = \mathbf{A}(\boldsymbol{\mu})\mathbf{R}_s\mathbf{A}^H(\boldsymbol{\mu}) + N_0\mathbf{I}_M,$$

where $\mathbf{y}[n]$ denotes the n -th column of \mathbf{Y} .

2.2 Hybrid Beamforming Architecture

We consider a narrow-band HAD combining architecture with N_{RF} RF chains, where $N_{\text{RF}} \ll M$, as illustrated in Fig. 1. The array output is processed by a two-stage combiner

$$\mathbf{W} \triangleq \mathbf{W}_{\text{RF}}\mathbf{W}_{\text{BB}} \in \mathbb{C}^{M \times N_{\text{RF}}},$$

where:

- $\mathbf{W}_{\text{RF}} \in \mathbb{C}^{M \times N_{\text{RF}}}$ is an analog RF combiner implemented using phase shifters. Its entries have constant modulus.
- $\mathbf{W}_{\text{BB}} \in \mathbb{C}^{N_{\text{RF}} \times N_{\text{RF}}}$ is a digital baseband combiner applied after the RF chains.

We assume a fully-connected analog network, so that each RF chain can access all M antennas through tunable phase shifters. This architecture enables us to adapt the effective combiner \mathbf{W} across training phases: during the coarse stage, all RF chains may be used to cover a broad angular range, whereas during the fine stage only a subset of RF chains needs to be active, focusing the combining pattern on previously identified sectors and reducing baseband power.

To exploit the structure of the ULA and facilitate implementation, we choose the columns of \mathbf{W}_{RF} from an M -point DFT dictionary. Let $\mathbf{w}_{\text{DFT}}(\gamma_\kappa) \in \mathbb{C}^M$ denote the κ -th DFT beam

steering vector, whose entries have unit modulus and whose spatial frequencies $\{\gamma_\kappa\}$ form a uniform grid on $[-\pi, \pi)$. The analog combiner is then formed by selecting N_{RF} columns from this DFT matrix:

$$\mathbf{W}_{\text{RF}} = [\mathbf{w}_{\text{DFT}}(\gamma_{\kappa_1}), \dots, \mathbf{w}_{\text{DFT}}(\gamma_{\kappa_{N_{\text{RF}}}})] \quad (2)$$

where $\{\kappa_1, \dots, \kappa_{N_{\text{RF}}}\} \subset \{1, \dots, M\}$ is the index set of the selected beams. The design of this index set, and of the digital combiner \mathbf{W}_{BB} , is the main focus of Section III.

2.3 Beamspace Signal Model and Problem Formulation

Applying the hybrid combiner to the received signal in (1) yields the beamspace measurements

$$\mathbf{Y}_b = \mathbf{W}^H \mathbf{Y} = \mathbf{A}_b(\boldsymbol{\mu}) \mathbf{S} + \mathbf{N}_b, \quad (3)$$

where $\mathbf{Y}_b \in \mathbb{C}^{N_{\text{RF}} \times N_{\text{snap}}}$, $\mathbf{N}_b \triangleq \mathbf{W}^H \mathbf{N}$ is the noise in beamspace, and

$$\mathbf{A}_b(\boldsymbol{\mu}) \triangleq \mathbf{W}^H \mathbf{A}(\boldsymbol{\mu}) \in \mathbb{C}^{N_{\text{RF}} \times d}$$

is the effective steering matrix after hybrid combining. Denote by $\mathbf{y}_b[n]$ the n -th column of \mathbf{Y}_b . The theoretical covariance matrix of the beamspace signal is

$$\mathbf{R}_b \triangleq \mathbb{E}\{\mathbf{y}_b[n] \mathbf{y}_b^H[n]\} = \mathbf{A}_b(\boldsymbol{\mu}) \mathbf{R}_s \mathbf{A}_b^H(\boldsymbol{\mu}) + \mathbf{R}_{n_b}, \quad (4)$$

where $\mathbf{R}_{n_b} \triangleq \mathbb{E}\{\mathbf{n}_b[n] \mathbf{n}_b^H[n]\}$ is the noise covariance in beamspace. When \mathbf{W}_{BB} is chosen with orthonormal columns and \mathbf{W}_{RF} has unit-modulus entries, \mathbf{R}_{n_b} is proportional to the identity and the noise remains white in beamspace. In practice we work with the sample covariance

$$\hat{\mathbf{R}}_b \triangleq \frac{1}{N_{\text{snap}}} \mathbf{Y}_b \mathbf{Y}_b^H.$$

The central problem addressed in this paper is twofold:

1. Given a constraint on the number of RF chains and DFT beams, design the effective combiner $\mathbf{W} = \mathbf{W}_{\text{RF}} \mathbf{W}_{\text{BB}}$ (equivalently, the subset of DFT beams and their digital weights) so that \mathbf{R}_b preserves the most informative part of \mathbf{R}_y for direction-of-arrival estimation.
2. Based on the reduced-dimensional beamspace measurements \mathbf{Y}_b , accurately estimate the spatial frequencies $\boldsymbol{\mu}$ using ESPRIT-type algorithms operating on a carefully selected subset of contiguous DFT beams.

In Section 3 we address these two tasks by first fitting a structured full-aperture covariance from a short training phase, and then using this covariance to guide the selection of contiguous DFT beams for a sparse beamspace Unitary ESPRIT estimator.

3 Covariance-Guided Coarse-to-Fine Beamspace ESPRIT

3.1 Coarse ESPRIT on a Virtual Element-Space Subarray

The first stage of our framework aims to obtain coarse spatial frequency estimates at low complexity, using only a short training phase and the existing HAD architecture. The key idea is to synthesize a virtual fully-digital ULA subarray of size N_{RF} that is centered at broadside, and to apply a standard covariance-based ESPRIT algorithm on the resulting element-space data.

We begin by defining the indices of the virtual subarray. Assuming for simplicity that M and N_{RF} share the same parity, we select a contiguous, centro-symmetric block of N_{RF} antennas around the array center:

$$\mathcal{M} \triangleq \left\{ m \in \{1, \dots, M\} : \left| m - \frac{M+1}{2} \right| \leq \frac{N_{\text{RF}} - 1}{2} \right\}. \quad (5)$$

Let $\mathbf{J}_{\mathcal{M}} \in \{0, 1\}^{N_{\text{RF}} \times M}$ denote the corresponding selection matrix, whose rows pick the entries of a vector associated with the indices in \mathcal{M} . For any $\mathbf{y}[n] \in \mathbb{C}^M$, the vector $\mathbf{y}_{\mathcal{M}}[n] \triangleq \mathbf{J}_{\mathcal{M}} \mathbf{y}[n]$ contains the samples observed at the virtual subarray, and the associated data matrix is

$$\mathbf{Y}_{\mathcal{M}} \triangleq \mathbf{J}_{\mathcal{M}} \mathbf{Y} \in \mathbb{C}^{N_{\text{RF}} \times N_{\text{snap}}}.$$

To realize this virtual subarray through the hybrid architecture, we exploit the freedom in the baseband combiner. Recall that the beamspace measurements are given by

$$\mathbf{Y}_{\text{b}} = \mathbf{W}^H \mathbf{Y} = \mathbf{W}_{\text{BB}}^H \mathbf{W}_{\text{RF}}^H \mathbf{Y}$$

with $\mathbf{W} = \mathbf{W}_{\text{RF}} \mathbf{W}_{\text{BB}}$. We choose the analog combiner \mathbf{W}_{RF} as in Section 2.2 (e.g., a subset of M -point DFT beams), and design the digital combiner \mathbf{W}_{BB} so that the effective hybrid combiner implements the virtual subarray. One convenient condition is

$$\mathbf{J}_{\mathcal{M}} \mathbf{W}_{\text{RF}} \mathbf{W}_{\text{BB}} = \mathbf{I}_{N_{\text{RF}}}, \quad (6)$$

which can be enforced by solving a small linear system for \mathbf{W}_{BB} once \mathbf{W}_{RF} is fixed and $\mathbf{J}_{\mathcal{M}} \mathbf{W}_{\text{RF}}$ is full rank. Under (6), the beamspace measurements \mathbf{Y}_{b} provide direct access to the virtual subarray data $\mathbf{Y}_{\mathcal{M}}$ (up to an invertible linear transform), and we can perform coarse DoA estimation in element space using $\mathbf{Y}_{\mathcal{M}}$.

We next outline the ESPRIT steps. From the virtual subarray data, we form the sample covariance

$$\hat{\mathbf{R}}_{\mathcal{M}} \triangleq \frac{1}{N_{\text{snap}}} \mathbf{Y}_{\mathcal{M}} \mathbf{Y}_{\mathcal{M}}^H.$$

To improve robustness to correlated sources and to exploit the centro-symmetry of the subarray, we apply forward-backward averaging and obtain

$$\hat{\mathbf{R}}_{\text{FBA}} = \frac{1}{2} [\hat{\mathbf{R}}_{\mathcal{M}} + \mathbf{\Pi}_{N_{\text{RF}}} \hat{\mathbf{R}}_{\mathcal{M}}^* \mathbf{\Pi}_{N_{\text{RF}}}], \quad (7)$$

where $\mathbf{\Pi}_{N_{\text{RF}}}$ is the $N_{\text{RF}} \times N_{\text{RF}}$ exchange (reversal) matrix. Let

$$\hat{\mathbf{R}}_{\text{FBA}} = \hat{\mathbf{U}} \hat{\mathbf{\Lambda}} \hat{\mathbf{U}}^H$$

denote the eigendecomposition of $\hat{\mathbf{R}}_{\text{FBA}}$, and let $\hat{\mathbf{U}}_{\text{S}} \in \mathbb{C}^{N_{\text{RF}} \times d}$ contain the d principal eigenvectors associated with the largest eigenvalues.

The core of ESPRIT is the rotational invariance of the signal subspace across two maximally overlapping subarrays. Let

$$\mathbf{J}_1 \triangleq [\mathbf{I}_{N_{\text{RF}}-1} \quad \mathbf{0}_{(N_{\text{RF}}-1) \times 1}], \quad \mathbf{J}_2 \triangleq [\mathbf{0}_{(N_{\text{RF}}-1) \times 1} \quad \mathbf{I}_{N_{\text{RF}}-1}]$$

be the selection matrices for the first and second shifted subarrays, respectively. The shift-invariance relation can be written as

$$\mathbf{J}_1 \hat{\mathbf{U}}_{\text{S}} \mathbf{\Psi} \approx \mathbf{J}_2 \hat{\mathbf{U}}_{\text{S}}, \quad (8)$$

where $\mathbf{\Psi} \in \mathbb{C}^{d \times d}$ is a nonsingular matrix encoding the spatial frequencies. A least-squares solution is given by

$$\hat{\mathbf{\Psi}} = (\mathbf{J}_1 \hat{\mathbf{U}}_{\text{S}})^\dagger \mathbf{J}_2 \hat{\mathbf{U}}_{\text{S}},$$

and the coarse spatial frequency estimates are obtained from the eigenvalues $\{\lambda_k\}$ of $\hat{\Psi}$ via

$$\hat{\mu}_{k,\text{coarse}} = \angle(\lambda_k), \quad k = 1, \dots, d.$$

Collecting these in the vector

$$\hat{\boldsymbol{\mu}}_{\text{coarse}} \triangleq [\hat{\mu}_{1,\text{coarse}}, \dots, \hat{\mu}_{d,\text{coarse}}]^T,$$

we obtain the coarse DoA estimates that will be refined in the subsequent covariance-fitting and beam-selection stages.

3.2 Source Power Estimation and Toeplitz-PSD Covariance Fitting

The coarse ESPRIT stage provides estimates of the spatial frequencies, collected in $\hat{\boldsymbol{\mu}}_{\text{coarse}}$. In this subsection we use these estimates to (i) obtain coarse source power and noise variance estimates and (ii) reconstruct a denoised, structured estimate of the full-aperture signal covariance. This covariance will later be used to guide the selection of DFT beams in beamspace.

We start from the forward-backward averaged sample covariance of the virtual subarray, $\hat{\mathbf{R}}_{\text{FBA}}$ in (7), and the parametric covariance model induced by (1). Restricting the model to the virtual subarray and substituting the coarse spatial frequencies yields

$$\mathbf{R}_{\mathcal{M}}(\mathbf{p}, N_0) \triangleq \mathbf{A}_{\mathcal{M}}(\hat{\boldsymbol{\mu}}_{\text{coarse}}) \text{diag}(\mathbf{p}) \mathbf{A}_{\mathcal{M}}^H(\hat{\boldsymbol{\mu}}_{\text{coarse}}) + N_0 \mathbf{I}_{N_{\text{RF}}},$$

where $\mathbf{A}_{\mathcal{M}}(\hat{\boldsymbol{\mu}}_{\text{coarse}})$ stacks the steering vectors of the virtual subarray, $\mathbf{p} = [p_1, \dots, p_d]^T$ contains the (unknown) source powers, and N_0 is the (unknown) noise variance. We estimate \mathbf{p} and N_0 by fitting this model to the empirical covariance. To avoid redundancy due to Hermitian symmetry, we gather the real and imaginary parts of the distinct entries of a Hermitian matrix into a real-valued vector via a linear operator $\text{vec}_H(\cdot)$. The power estimation task is then cast as the non-negative least-squares problem

$$\min_{\mathbf{p} \geq \mathbf{0}, N_0 \geq 0} \left\| \text{vec}_H(\hat{\mathbf{R}}_{\text{FBA}}) - \text{vec}_H(\mathbf{R}_{\mathcal{M}}(\mathbf{p}, N_0)) \right\|_2^2. \quad (9)$$

This problem has $d + 1$ real unknowns and can be written in standard real-valued quadratic-program (QP) form with simple non-negativity constraints. In our implementation we solve (9) using an off-the-shelf NNLS/QP solver and obtain coarse estimates $\hat{\mathbf{p}}_{\text{coarse}}$ and $\hat{N}_{0,\text{coarse}}$.

Next we reconstruct and denoise an estimate of the full-aperture signal covariance. Using the coarse powers and spatial frequencies, we form the model-based signal covariance on the full array,

$$\hat{\mathbf{R}}_s \triangleq \mathbf{A}(\hat{\boldsymbol{\mu}}_{\text{coarse}}) \text{diag}(\hat{\mathbf{p}}_{\text{coarse}}) \mathbf{A}^H(\hat{\boldsymbol{\mu}}_{\text{coarse}}) \in \mathbb{C}^{M \times M},$$

which corresponds to the signal-only part of the covariance after subtracting the estimated noise power. For a ULA with uncorrelated sources and spatially white noise, the ideal signal covariance is Hermitian Toeplitz and positive semidefinite. To exploit this structure and reduce sampling noise, we project $\hat{\mathbf{R}}_s$ onto the cone of Hermitian Toeplitz positive-semidefinite (Toeplitz-PSD) matrices of dimension M by solving

$$\tilde{\mathbf{R}}_s = \arg \min_{\mathbf{R} \in \mathcal{T}^+} \|\mathbf{R} - \hat{\mathbf{R}}_s\|_F^2, \quad (10)$$

where \mathcal{T}^+ denotes the set of Hermitian Toeplitz PSD matrices of dimension M . Parameterizing \mathbf{R} by its first column and separating real and imaginary parts leads to a small real-valued QP in the Toeplitz coefficients, which we solve numerically.¹ The resulting matrix $\tilde{\mathbf{R}}_s$ serves as a denoised proxy for the signal covariance on the full aperture and implicitly captures both the coarse spatial frequencies and their estimated powers.

¹An explicit real-valued QP formulation for both (9) and (10) is given in Appendix A.

In summary, this stage produces coarse estimates of the source powers and noise variance, together with a structured, denoised estimate $\tilde{\mathbf{R}}_s$ of the signal covariance. In Section 3.3 we will use $\tilde{\mathbf{R}}_s$ to score and select contiguous DFT beam subsets for the fine-resolution beamspace ESPRIT stage.

3.3 Covariance-Guided DFT Beam Selection

The coarse spatial frequency estimates provide a rough location of the sources. The goal of this stage is to select, for each sector of interest, a small contiguous set of DFT beams that preserves the most informative part of the reconstructed signal covariance while respecting the contiguity and beam-budget constraints required by beamspace ESPRIT. We use the denoised full-aperture signal covariance $\tilde{\mathbf{R}}_s \in \mathbb{C}^{M \times M}$ obtained in Section 3.2 as a proxy for the underlying array response.

We proceed in two main steps. First, we group the coarse estimates into angular sectors. Second, within each sector we score and select contiguous DFT beam sets based on covariance capture and numerical conditioning.

Sectorization and sector-wise beam pools Following the sliding-window sectorization idea of [18], we partition the coarse estimates $\hat{\boldsymbol{\mu}}_{\text{coarse}}$ into G disjoint sectors, each associated with one sector of interest (SoI). Each sector is mapped to a set of DFT beams whose mainlobes cover the corresponding angular interval. Denoting by $\mathbf{B} = [\mathbf{b}_1, \dots, \mathbf{b}_M] \in \mathbb{C}^{M \times M}$ the phase-shifted DFT beamforming matrix, we obtain for sector g a sorted index set

$$\mathcal{B}_g \subset \{1, \dots, M\}, \quad g = 1, \dots, G,$$

where \mathcal{B}_g contains the DFT beam indices associated with the g -th SoI. The sets $\{\mathcal{B}_g\}$ form sector-wise beam pools from which we will select the fine-stage beams.

Candidate beam sets and covariance-capture score Within each sector \mathcal{B}_g , we seek one contiguous block of $K_g \geq 2$ DFT beams

$$\mathcal{S}_g = \{\kappa_j, \kappa_{j+1}, \dots, \kappa_{j+K_g-1}\} \subset \mathcal{B}_g,$$

that is most informative for the sources in the g -th sector. For a given candidate \mathcal{S}_g , we collect the corresponding beamformers into

$$\mathbf{B}_g(\mathcal{S}_g) \triangleq [\mathbf{b}_{\kappa_j}, \mathbf{b}_{\kappa_{j+1}}, \dots, \mathbf{b}_{\kappa_{j+K_g-1}}] \in \mathbb{C}^{M \times K_g},$$

and define the associated Gram matrix

$$\mathbf{G}_g(\mathcal{S}_g) \triangleq \mathbf{B}_g(\mathcal{S}_g)^H \mathbf{B}_g(\mathcal{S}_g) \in \mathbb{C}^{K_g \times K_g}.$$

The denoised covariance $\tilde{\mathbf{R}}_s$ provides a measure of how much signal energy is captured by the subspace spanned by the beams in \mathcal{S}_g . Motivated by first-order MSE expressions for ESPRIT in DFT beamspace [19], we quantify this via the covariance-capture score

$$\text{cap}(\mathcal{S}_g) = \text{tr} \left[(\mathbf{G}_g(\mathcal{S}_g) + \gamma \mathbf{I}_{K_g})^{-1} \mathbf{B}_g(\mathcal{S}_g)^H \tilde{\mathbf{R}}_s \mathbf{B}_g(\mathcal{S}_g) \right], \quad (11)$$

where $\gamma \geq 0$ is a small Tikhonov parameter that improves numerical stability when $\mathbf{G}_g(\mathcal{S}_g)$ is nearly singular. This quantity can be interpreted as the signal covariance preserved after least-squares projection onto the span of $\mathbf{B}_g(\mathcal{S}_g)$.

To discourage highly ill-conditioned beam sets, we also measure the squared condition number

$$\kappa_g^2(\mathcal{S}_g) \triangleq \text{cond}(\mathbf{G}_g(\mathcal{S}_g))^2,$$

and define the final score as

$$\text{score}(\mathcal{S}_g) = \frac{\text{cap}(\mathcal{S}_g)}{1 + \alpha \kappa_g^2(\mathcal{S}_g)},$$

where $\alpha \geq 0$ is a design parameter that trades off signal capture and numerical robustness. In our simulations we keep α fixed across all sectors and SNRs.

For wide sectors, enumerating all possible contiguous K_g -beam windows in \mathcal{B}_g may be computationally expensive. To reduce complexity, we optionally prune candidates using the beamspace power profile

$$\rho_m \triangleq [\mathbf{B}^H \tilde{\mathbf{R}}_s \mathbf{B}]_{mm}, \quad m = 1, \dots, M.$$

For each sector \mathcal{B}_g , we retain only those windows that contain at least one of the beams with the largest values of $\{\rho_m : m \in \mathcal{B}_g\}$, which concentrates the search around beams that already appear strong in the reconstructed covariance.

Finally, for each sector we select the best beam set by solving

$$\mathcal{S}_g^* = \arg \max_{\mathcal{S}_g \subset \mathcal{B}_g, |\mathcal{S}_g|=K_g} \text{score}(\mathcal{S}_g),$$

with ties broken in favour of smaller condition number and more central windows within \mathcal{B}_g . The union

$$\mathcal{K}_{\text{fine}} \triangleq \bigcup_{g=1}^G \mathcal{S}_g^* \subset \{1, \dots, M\}$$

defines the DFT beams used by the fine-stage RF combiner in Section 3.4. A detailed pseudocode description of this covariance-guided beam selection pipeline is provided in Algorithm 1 in Appendix B.

3.4 Fine Spatial Frequency Estimation via Sparse Beamspace Unitary ESPRIT

Given the covariance-guided beam selection in Section 3.3, the fine-stage RF combiner is constructed from the union of selected DFT beams

$$\mathcal{K}_{\text{fine}} \triangleq \bigcup_{g=1}^G \mathcal{S}_g^* \subset \{1, \dots, M\},$$

where each \mathcal{S}_g^* is a contiguous K_g -beam subset inside the g -th sector. The corresponding fine-stage beamspace observation is

$$\mathbf{Y}_b \in \mathbb{C}^{N_{\text{RF}}^{\text{fine}} \times N_{\text{snap}}}, \quad N_{\text{RF}}^{\text{fine}} = |\mathcal{K}_{\text{fine}}|,$$

obtained by projecting the array data \mathbf{Y} onto the DFT beams indexed by $\mathcal{K}_{\text{fine}}$.

In contrast to classical 1-D ESPRIT in DFT beamspace, the index set $\mathcal{K}_{\text{fine}}$ is generally sparse: it consists of a few disjoint contiguous blocks, each contained in a different sector, rather than of a single full-aperture block. As a result, the standard shift-selection matrices that connect every pair of consecutive beams are no longer appropriate. Instead, we exploit only those forward beam pairs that are actually present in $\mathcal{K}_{\text{fine}}$ and construct a sparse invariance equation tailored to this reduced beamspace.

We follow the real-valued Unitary ESPRIT approach to exploit centro-symmetry and forward-backward averaging. From the fine-stage beamspace data \mathbf{Y}_b we form the real-valued matrix

$$\mathbf{Y}_{\text{UE}} = \sqrt{2}[\Re\{\mathbf{Y}_b\} \quad \Im\{\mathbf{Y}_b\}] \in \mathbb{R}^{N_{\text{RF}}^{\text{fine}} \times 2N_{\text{snap}}}, \quad (12)$$

which is equivalent to applying forward-backward averaging and a left- $\mathbf{\Pi}$ -real transform to the complex beamspace data [19]. We then compute a rank- d signal subspace from \mathbf{Y}_{UE} , for

example by performing an SVD and retaining the d dominant left singular vectors. Denoting this matrix by $\mathbf{U}_S \in \mathbb{R}^{N_{\text{RF}}^{\text{fine}} \times d}$, each of its rows corresponds to one selected DFT beam in $\mathcal{K}_{\text{fine}}$.

To construct the sparse shift-invariance equations, we sort the indices in $\mathcal{K}_{\text{fine}}$ in ascending order and denote them by

$$\mathcal{K}_{\text{fine}} = \{\ell_1, \dots, \ell_{N_{\text{RF}}^{\text{fine}}}\}, \quad \ell_1 < \dots < \ell_{N_{\text{RF}}^{\text{fine}}}.$$

We then define the set of admissible forward beam pairs

$$\mathcal{P} \triangleq \{(\ell_r, \ell_{r+1}) : \ell_{r+1} = \ell_r + 1, r = 1, \dots, N_{\text{RF}}^{\text{fine}} - 1\},$$

which contains exactly those adjacent DFT beam indices that form valid shift-invariant pairs. For each $(i, j) \in \mathcal{P}$ we introduce row-selection vectors that pick the corresponding rows of \mathbf{U}_S , and stack them into selection matrices

$$\mathbf{J}_1, \mathbf{J}_2 \in \{0, 1\}^{|\mathcal{P}| \times N_{\text{RF}}^{\text{fine}}},$$

so that $\mathbf{J}_1 \mathbf{U}_S$ contains the rows associated with the “first” beams in all pairs $(i, j) \in \mathcal{P}$ and $\mathbf{J}_2 \mathbf{U}_S$ contains the corresponding “second” beams. The sparse shift-invariance relation can then be written as

$$\mathbf{J}_1 \mathbf{U}_S \mathbf{\Phi} \approx \mathbf{J}_2 \mathbf{U}_S,$$

where $\mathbf{\Phi} \in \mathbb{C}^{d \times d}$ is a nonsingular matrix that encodes the spatial frequencies. A least-squares estimate is obtained as

$$\hat{\mathbf{\Phi}} = (\mathbf{J}_1 \mathbf{U}_S)^\dagger \mathbf{J}_2 \mathbf{U}_S,$$

and the fine spatial frequency estimates follow from the eigenvalues $\{\lambda_k\}$ of $\hat{\mathbf{\Phi}}$ via

$$\hat{\mu}_{k,\text{fine}} = \angle(\lambda_k), \quad k = 1, \dots, d.$$

Collecting these estimates in

$$\hat{\boldsymbol{\mu}}_{\text{fine}} \triangleq [\hat{\mu}_{1,\text{fine}}, \dots, \hat{\mu}_{d,\text{fine}}]^T,$$

we obtain the final DoA estimates reported in the numerical results. Since $N_{\text{RF}}^{\text{fine}}$ is small by design, the SVD, least-squares step, and eigen-decomposition are of low dimension and incur negligible additional complexity compared with the coarse stage.

4 Numerical Results

4.1 Experimental Setup

We consider a ULA with $M=32$ sensors and $d=3$ uncorrelated sources. The broadside-normalized spatial frequencies are fixed to

$$\boldsymbol{\mu}_{\text{true}} = [-2.1, 0.5, 2.5]^\top \text{ rad},$$

and the source power vector is

$$\mathbf{p} = [0.95, 0.5, 0.1]^\top, \quad \mathbf{R}_s = \text{diag}(\mathbf{p}).$$

Each experiment uses $N_{\text{snap}}=100$ snapshots and circularly symmetric complex Gaussian noise with one-sided power spectral density N_0 .

We report performance versus the array SNR (ASNR) in dB, defined by

$$\text{ASNR} \triangleq 10 \log_{10} \left(\frac{\text{tr}(\mathbf{A}(\boldsymbol{\mu}_{\text{true}}) \mathbf{R}_s \mathbf{A}^H(\boldsymbol{\mu}_{\text{true}}))}{M N_0} \right) = 10 \log_{10} \left(\frac{\sum_{k=1}^d p_k}{N_0} \right) \text{ dB}, \quad (13)$$

where $\mathbf{A}(\boldsymbol{\mu})$ is the array steering matrix defined in Section 2.

We compare five pipelines:

1. **Proposed coarse stage (centro-symmetric mask):** element-space TLS-ESPRIT on the centro-symmetric mask described in Section 3.1.
2. **Coarse stage from [18] (non-symmetric mask):** element-space TLS-ESPRIT on the contiguous, non-symmetric mask used in the Tensor-ESPRIT framework.
3. **Proposed fine stage:** proposed coarse stage in (1) followed by the covariance-guided beam selection of Section 3.3 with $K_g=2$ beams per sector and sparse beamspace Unitary ESPRIT (Section 3.4).
4. **Fine stage from [18]:** coarse stage in (2) followed by the sectorization-based beam selection of [18] with $K_g=2$ beams per sector and the same fine ESPRIT estimator.
5. **Oracle beams:** identical to (3) but using, at the fine stage, the “oracle” DFT beams whose supports are closest to the true source directions, as in [19].

RF-chain allocation across stages. Unless otherwise stated, the coarse stage uses $N_{\text{RF}}^{\text{coarse}}=12$ RF chains, while the fine stage uses $N_{\text{RF}}^{\text{fine}}=6$ active DFT beams. In the ablations we vary this fine-stage beam budget while keeping N_{snap} fixed to study accuracy–runtime trade-offs.

Evaluation metrics. We evaluate four main metrics.

- (i) Root mean-square error (RMSE) of the spatial-frequency estimates in radians:

$$\text{RMSE} \triangleq \sqrt{\mathbb{E} \left\{ \frac{1}{d} \sum_{k=1}^d (\hat{\mu}_k - \mu_{\text{true},k})^2 \right\}}, \quad (14)$$

where $\hat{\mu}_k$ denotes the fine-stage estimate of $\mu_{\text{true},k}$. In the Monte Carlo simulations we approximate (14) by averaging over $R=10^4$ independent trials.

- (ii) Stochastic Cramér–Rao bound (CRB) for the spatial-frequency vector $\boldsymbol{\mu}$. We use the Gaussian data model in (1) with known source covariance and noise variance and compute the Fisher information matrix $\mathbf{J}(\boldsymbol{\mu})$ as in [22]. We summarize the bound by

$$\text{CRB}(\boldsymbol{\mu}) \triangleq \frac{1}{d} \text{tr}(\mathbf{J}(\boldsymbol{\mu})^{-1}), \quad (15)$$

and plot $\sqrt{\text{CRB}(\boldsymbol{\mu})}$ as a reference in the RMSE figures, together with the gap-to-CRB in dB defined as $10 \log_{10}(\text{RMSE}/\sqrt{\text{CRB}})$.

- (iii) Failure rate, defined relative to a CRB-based threshold:

$$P_{\text{fail}} \triangleq \mathbb{P} \left(\max_k |\hat{\mu}_k - \mu_{\text{true},k}| > k_{\text{thr}} \sqrt{\text{CRB}(\boldsymbol{\mu})} \right), \quad (16)$$

with threshold factor $k_{\text{thr}}=3$. In the plots we estimate P_{fail} via the empirical fraction of failures across trials and report Wilson 95% confidence intervals per ASNR.

- (iv) Largest principal angle (LPA) between the true and estimated signal subspaces in degrees. Let \mathbf{U}_S and $\hat{\mathbf{U}}_S$ contain orthonormal bases for the true and estimated d -dimensional signal subspaces, respectively. The LPA is defined as

$$\text{LPA} \triangleq \cos^{-1} \left(\sigma_{\max}(\mathbf{U}_S^H \hat{\mathbf{U}}_S) \right), \quad (17)$$

where $\sigma_{\max}(\cdot)$ denotes the largest singular value. This metric quantifies subspace alignment and helps interpret how improved beam selection tightens the signal subspace.

All performance curves are obtained from $R=10^4$ Monte Carlo trials, with independent noise realizations across trials and ASNRs. We reuse the same random seeds across methods to enable pairwise comparisons.

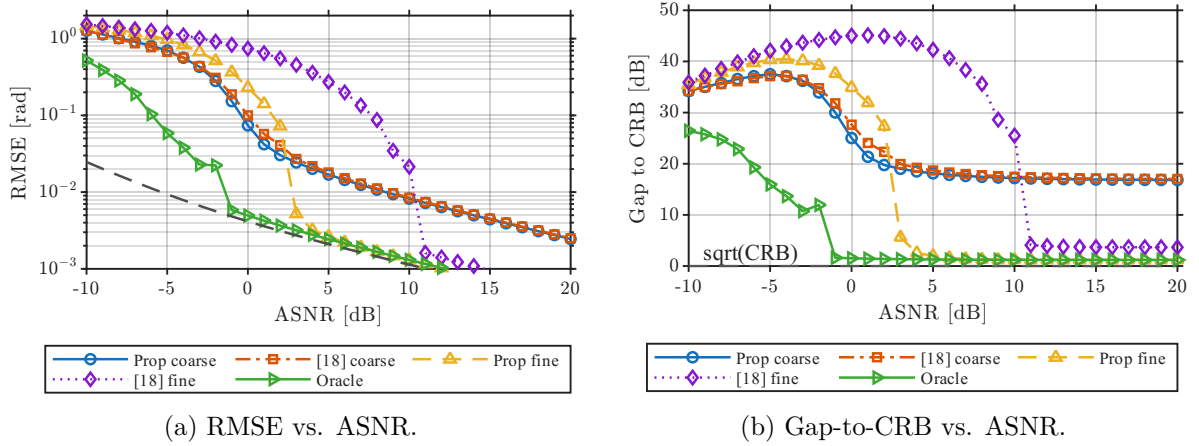


Figure 2: Angle estimation performance versus ASNR for $N_{\text{RF}}^{\text{coarse}} = 12 \rightarrow N_{\text{RF}}^{\text{fine}} = 6$: (a) RMSE; (b) gap to the CRB.

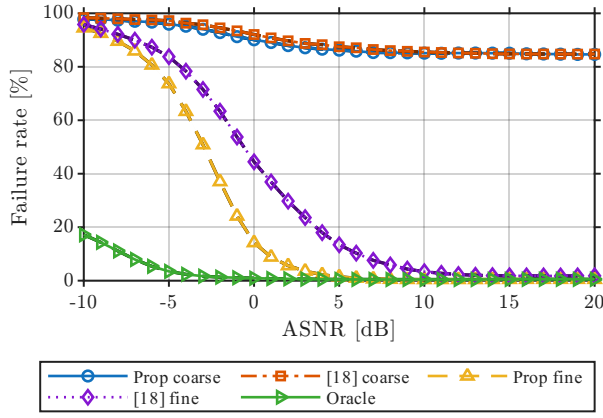
4.2 Main results

RMSE and gap-to-CRB. Figure 2 shows RMSE and gap-to-CRB versus ASNR for $N_{\text{RF}}^{\text{coarse}}=12$ and $N_{\text{RF}}^{\text{fine}}=6$. The two coarse-only baselines (centro-symmetric mask vs. non-symmetric mask) exhibit similar trends and remain several dB away from the CRB across the SNR range, as expected from the reduced aperture. By contrast, the proposed covariance-guided fine stage yields a pronounced improvement: the RMSE curve closely tracks that of the oracle beam configuration, and the gap-to-CRB remains within approximately 1–2 dB for $\text{ASNR} \geq 4$ dB. The sectorization-based fine stage from [18] also improves over the coarse estimates, but requires roughly 4–6 dB higher ASNR to reach a comparable near-CRB regime. This shows that the proposed beam selection extracts more information per active beam under the same RF-chain budget.

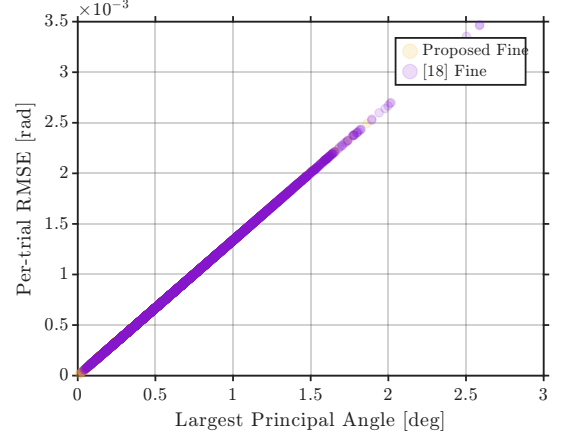
Reliability and threshold behaviour. Figure 3a reports failure probabilities as a function of ASNR using the CRB-based threshold in (16). The proposed fine stage achieves less than 10% failure probability already around 0–1 dB, whereas the fine stage of [18] requires approximately 5–6 dB to reach a similar reliability level. At high ASNR both fine-stage pipelines eventually approach zero failures, but the covariance-guided selector enters the reliable regime much earlier. This behaviour is consistent with the smaller performance gap to the oracle in Fig. 2.

Subspace alignment. Figure 3b plots the scatter of LPA versus estimation error at $\text{ASNR} = 15$ dB for the proposed fine stage and the sectorization-based fine stage. The points lie close to a nearly linear trend, with Pearson correlation coefficient close to one, indicating that the largest principal angle is an informative proxy for estimation quality. The proposed method yields consistently smaller LPAs and errors than the sectorization baseline, highlighting that covariance-guided beam tuning improves the alignment between the true and estimated signal subspaces.

Distributional shape. ECDFs in Fig. 4 show the distribution of per-trial estimation errors at $\text{ASNR} = -5, 0, 5, 15$ dB. At low ASNR (−5 and 0 dB), the error distribution of the proposed fine stage dominates that of the sectorization-based fine stage in the sense of first-order stochastic dominance: for any fixed error threshold, the proposed method yields a smaller fraction of large-error trials. At higher ASNR (5 and 15 dB), both fine stages concentrate near zero error, but the proposed method remains uniformly left-shifted, reflecting improved high-quantile performance



(a) Failure rates vs. ASNR.



(b) LPA-error scatter at ASNR = 15 dB.

Figure 3: Reliability behaviour and subspace alignment: (a) Failure rates vs. ASNR; (b) LPA-error scatter at ASNR = 15 dB.

(e.g., lower 90th percentile error). The oracle beams provide a consistent lower bound across all SNRs.

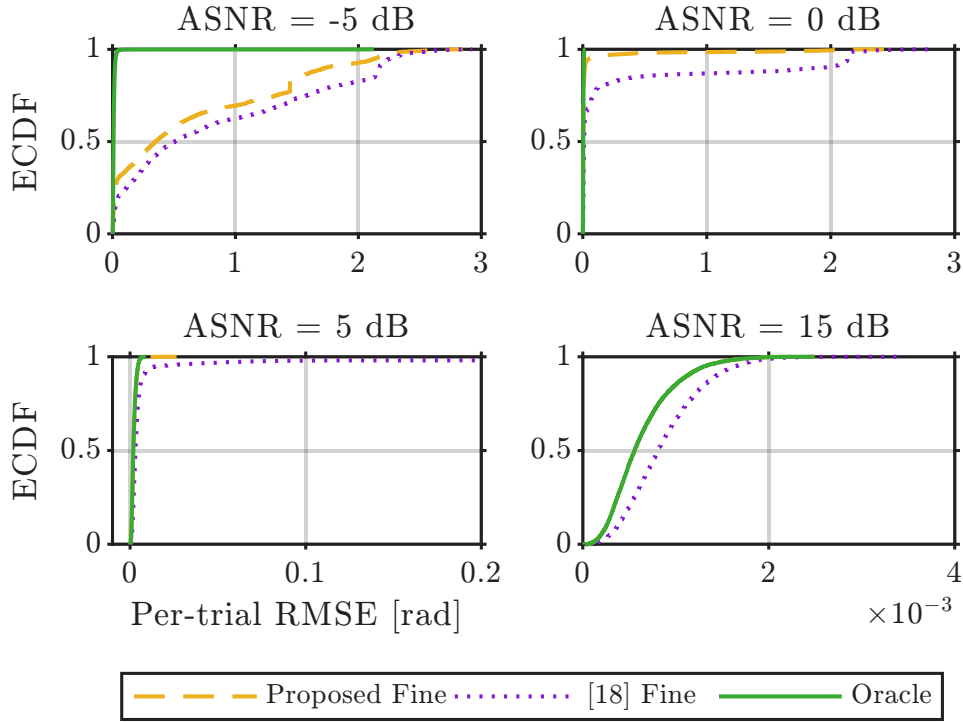


Figure 4: ECDFs of error at ASNR = -5, 0, 5, 15 dB.

4.3 Ablations and stress tests

To isolate the sources of performance gains, we include three ablations: (i) accuracy-runtime trade-off under a dynamic RF (beam) budget, (ii) sector-edge stress test with two sources, and (iii) fixed fine-stage beam budget $K_g=K_f$ comparing covariance-guided selection with pure sectorization.

Accuracy–runtime trade-off under a dynamic RF budget. In the first ablation we vary the fine-stage beam budget while keeping the coarse stage fixed at $N_{\text{RF}}^{\text{coarse}}=12$. We consider four configurations:

$$\text{Cov } 12 \rightarrow 6, \quad \text{Cov } 12 \rightarrow 12, \quad \text{Sect } 12 \rightarrow 6, \quad \text{Sect } 12 \rightarrow 12,$$

where “Cov” denotes the covariance-guided selector and “Sect” denotes the sectorization baseline from [18]. For each configuration we measure the median runtime of the covariance-fitting stage, the fine-stage beam selection, and the fine ESPRIT call, together with the resulting DOA RMSE.

The timing and accuracy data in Table 1 show that the proposed covariance-guided configurations lie on or near the Pareto frontier in the RMSE–runtime plane. The setting “Cov 12→6” already reaches a near-CRB regime with modest additional cost over sectorization, while “Cov 12→12” provides the highest accuracy at a moderate increase in runtime. In contrast, sectorization-based configurations either incur substantially larger RMSE for similar runtime or require more beams to approach the same accuracy.

Table 1: Median runtime and DOA RMSE for the four fine-stage configurations in the dynamic RF-budget ablation. The coarse stage uses $N_{\text{RF}}^{\text{coarse}} = 12$ RF chains, while the fine stage is constrained to either 6 or 12 active DFT beams. Timings are medians over 10^4 Monte Carlo trials.

Configuration	ASNR [dB]	RMSE [rad]	t_{cov} [ms]	t_{sel} [ms]	t_{ES} [ms]	t_{total} [ms]
Cov 12→6	3	0.015512	2.0945	0.86825	0.36675	3.3961
Cov 12→6	6	0.0024718	2.0889	0.86995	0.36560	3.4057
Cov 12→12	3	0.028267	2.0982	0.73865	0.42450	3.3275
Cov 12→12	6	0.0063330	2.1107	0.73895	0.42245	3.3426
Sect 12→6	3	0.45542	1.8838	0.26605	0.23610	2.4263
Sect 12→6	6	0.19915	1.8861	0.26685	0.23605	2.4278
Sect 12→12	3	0.014777	1.9030	0.27000	0.29430	2.5057
Sect 12→12	6	0.0063796	1.9008	0.27055	0.29010	2.5061

At ASNR = 3 dB, the Pareto plot in Fig. 5 indicates that “Cov 12→6” offers the best runtime–accuracy compromise, whereas “Cov 12→12” pushes closer to the oracle at slightly higher cost. At ASNR = 6 dB, all four methods lie near the frontier, but the sectorization-based options remain dominated in terms of RMSE for a given runtime or offer comparable accuracy at a higher computational cost.

Sector-edge stress test with two sources. In the second ablation we stress-test robustness near sector boundaries. We consider $d=2$ uncorrelated sources with power vector

$$\mathbf{p} = [p_1, p_2]^T = [0.95, 0.5]^T, \quad \mathbf{R}_s = \text{diag}(\mathbf{p}),$$

and spatial frequencies $\boldsymbol{\mu} = [\mu_1, \mu_2]^T$. The first source is fixed at $\mu_1 = -2.1$, while the second source is swept across the boundary between two adjacent DFT beams. Let κ_{bdy} and $\kappa_{\text{bdy}}+1$ denote the corresponding DFT beam indices with spatial frequencies $\gamma_{\kappa_{\text{bdy}}}$ and $\gamma_{\kappa_{\text{bdy}}+1}$. We define the boundary spatial frequency

$$\mu_{\text{edge}} \triangleq \frac{1}{2}(\gamma_{\kappa_{\text{bdy}}} + \gamma_{\kappa_{\text{bdy}}+1}),$$

and parameterize the displacement of the second source by $\delta \triangleq \mu_2 - \mu_{\text{edge}}$. The horizontal axis in Figs. 6a and 6b is normalized as $\delta/(w_{\text{sec}}/2)$, where w_{sec} is the sector width.

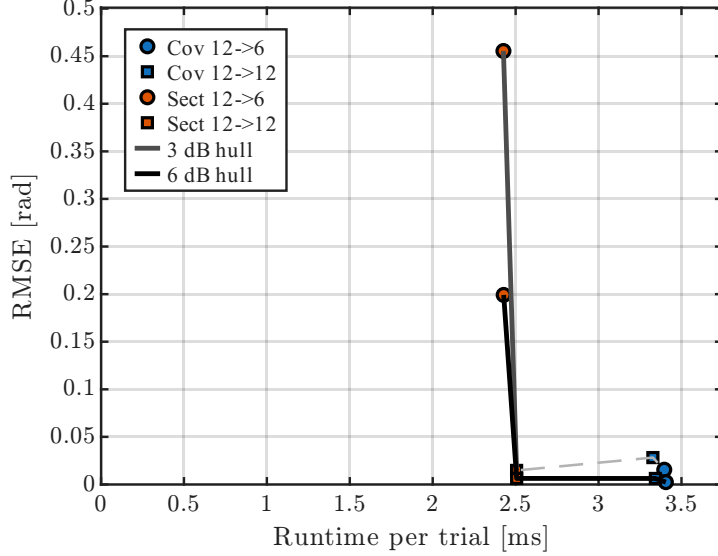


Figure 5: Pareto trade-off between median runtime per Monte Carlo trial and DOA RMSE for the four fine-stage configurations. Timings include covariance fitting, fine-stage beam selection, and the fine ESPRIT step.

The coarse stage again uses $N_{\text{RF}}^{\text{coarse}}=12$ RF chains and TLS-ESPRIT on the centro-symmetric mask. For the fine stage we compare the proposed covariance-guided selector with the sectorization baseline at beam budget $K_f=2$, both followed by beamspace Unitary ESPRIT.

Figure 6a plots the RMSE of the spatial-frequency estimates versus the normalized boundary offset at ASNR = 3 and 6 dB. The sectorization baseline exhibits a broad region of large error around the boundary and does not approach the CRB for any offset in the low-SNR case. In contrast, the covariance-guided beams keep the RMSE close to the CRB across most offsets and substantially reduce the peak error at the boundary. The corresponding failure probabilities in Fig. 6b show a similar trend: the sectorization-based fine stage saturates near 100% failures for a wide range of offsets, whereas the proposed method maintains low failure rates except in a narrow neighbourhood of the exact boundary. These results indicate that once the fine beams are selected in a data-aware manner, the residual sensitivity at sector edges is mainly due to the coarse-sector definition rather than an intrinsic limitation of ESPRIT in beamspace.

Fixed fine-stage beam budget $K_g = K_f$: covariance-guided selection vs. pure sectorization. In the third ablation we fix the fine-stage beam budget and compare only the beam-selection mechanisms. We set $K_f \in \{2, 3, 4\}$ and evaluate the DOA RMSE and failure probabilities for the covariance-guided selector and for pure sectorization, using the same coarse stage as before.

Figure 7a shows RMSE versus ASNR, together with the CRB, for the three beam budgets. The covariance-guided selector with $K_f = 2$ already enters a near-CRB regime, while the sectorization baseline with the same budget exhibits substantially larger RMSE across most ASNR values. Increasing K_f to 3 or 4 further reduces the gap to the CRB for the proposed method, whereas sectorization requires larger beamsets to achieve comparable performance and remains less efficient per active beam. The failure statistics in Fig. 7b confirm this picture. For $K_f = 2$, the proposed method achieves low failure rates already at moderate SNR, while sectorization remains failure-dominated over a broad ASNR range. Allowing larger beamsets ($K_f = 3$ or 4) benefits both methods, but the covariance-guided selector consistently maintains a substantially lower failure probability for the same beam budget. This supports using $K_f = 2$ as the default fine-stage budget and only increasing K_f in scenarios where the application can

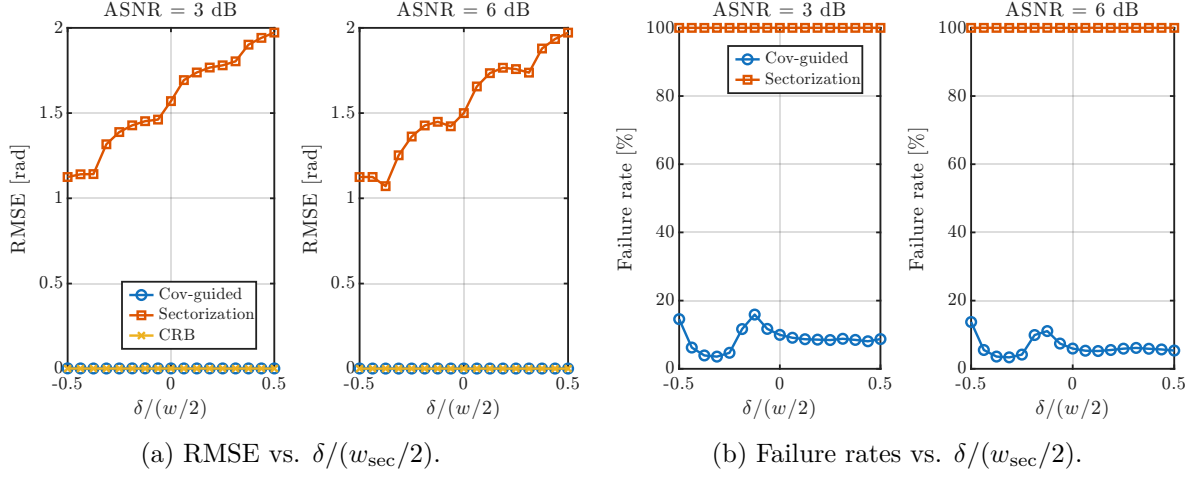


Figure 6: Sector-edge stress test with two paths for the normalized boundary offset $\delta/(w_{\text{sec}}/2)$. The setup is the same as Fig. 2. Results are shown for left: ASNR = 3 dB and right: ASNR = 6 dB: (a) RMSE vs. $\delta/(w_{\text{sec}}/2)$; (b) Failure rates vs. $\delta/(w_{\text{sec}}/2)$.

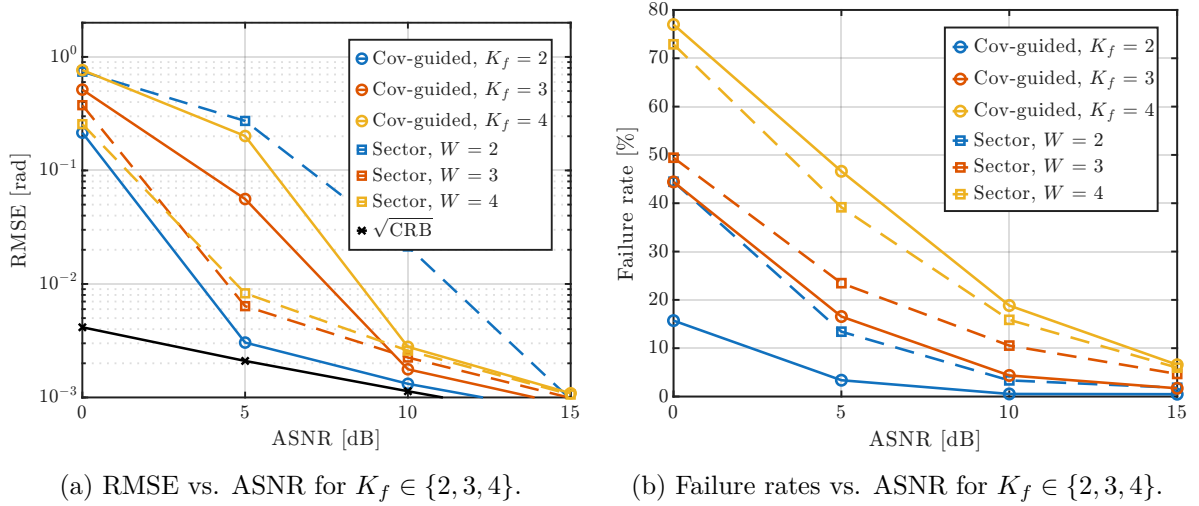


Figure 7: The proposed covariance-guided selector and the pure sectorization baseline for $K_f \in \{2, 3, 4\}$: (a) RMSE vs. ASNR; (b) Failure rates vs. ASNR.

tolerate higher runtime in exchange for marginal accuracy gains.

5 Conclusion

We have proposed a two-stage spatial frequency estimation framework for hybrid analog/digital mmWave MIMO receivers that employ DFT beamspace processing under a strict RF-chain budget. Starting from hybrid measurements, we synthesize a virtual fully-digital centro-symmetric subarray and apply element-space ESPRIT to obtain coarse spatial frequency estimates. Using these estimates, we form a full-aperture signal covariance and project it onto the Toeplitz-PSD cone, and we use the resulting denoised covariance to select, in each coarse sector, a small contiguous block of DFT beams under an explicit beam budget. The selected beams feed a sparse beamspace Unitary ESPRIT stage, so that the overall complexity is dominated by a single low-dimensional ESPRIT call while preserving a large effective aperture.

Monte Carlo results for a 32-element ULA with three paths show that the covariance-guided beam selector substantially improves the accuracy-complexity trade-off compared with a sliding-

window sectorization baseline built on the same DFT codebook and ESPRIT estimator. In particular, the proposed method attains near-Cramér–Rao bound MSE at moderate ASNRs while markedly reducing the outlier probability according to a CRB-scaled failure metric. Pareto plots of RMSE versus runtime indicate that, for a given RF beam budget, the covariance-guided design dominates sectorization across a broad ASNR range, and that the effective aperture can be retained with only a few carefully chosen beams per sector. Sector-edge stress tests further show that the data-driven beam selection is less sensitive to coarse-sector misalignment and yields more stable performance when dominant paths lie near sector boundaries.

Beyond quantitative gains, the numerical study provides several qualitative insights for the hybrid beamspace DoA estimation. First, fitting a structured signal-plus-noise covariance and using it to drive beam selection is more informative than relying solely on coarse point estimates or raw beam powers, because the covariance encodes both the signal subspace and the relative path powers and acts as an implicit denoiser. Second, the results confirm that carefully chosen groups of adjacent DFT beams can emulate larger effective apertures, so that hybrid receivers can approach element-space resolution when the beam budget and sector geometry are well matched. Third, the ablations over the fine-stage beam budget show diminishing returns beyond a small number of beams per sector, which provides a practical guideline for RF resource allocation in dynamic beam-budget scenarios.

Several directions remain open for future research. A natural extension is to generalize the covariance-guided beam selection to two-dimensional and three-dimensional array geometries, enabling joint azimuth–elevation estimation in uniform rectangular or more irregular arrays. Another promising direction is to incorporate wideband and near-field effects, including beam squint and range dependence, by coupling the proposed covariance-fitting stage with tensor-based or parametric wideband ESPRIT variants. Robust extensions that account for model mismatch, spatially colored noise, or a small number of strong interferers via alternative divergence measures or robust M-estimation are also of interest. Finally, learning-aided variants that use the proposed covariance-fitting and beam-selection scheme as a teacher for lightweight neural beam selectors, and that exploit temporal correlation in tracking scenarios, could further reduce training overhead and latency in beyond-5G and 6G hybrid MIMO systems.

A Real-Valued Quadratic-Program Formulations

In this appendix we detail the real-valued quadratic-program (QP) formulations used in the power and noise-variance estimation step (9) and in the Toeplitz–PSD covariance projection (10).

A.1 Power and Noise-Variance Estimation

Recall the model-based covariance of the virtual subarray,

$$\mathbf{R}_{\mathcal{M}}(\mathbf{p}, N_0) = \mathbf{A}_{\mathcal{M}}(\hat{\boldsymbol{\mu}}_{\text{coarse}}) \text{diag}(\mathbf{p}) \mathbf{A}_{\mathcal{M}}^H(\hat{\boldsymbol{\mu}}_{\text{coarse}}) + N_0 \mathbf{I}_{N_{\text{RF}}}$$

with unknown power vector $\mathbf{p} \in \mathbb{R}^d$ and noise variance $N_0 \in \mathbb{R}$. Let

$$\mathbf{x} \triangleq \begin{bmatrix} \mathbf{p} \\ N_0 \end{bmatrix} \in \mathbb{R}^{d+1}, \quad \mathbf{x} \geq \mathbf{0},$$

and denote by $\hat{\mathbf{R}}_{\text{FBA}}$ the empirical FBA covariance in (7).

We collect the real and imaginary parts of the distinct entries of a Hermitian $N_{\text{RF}} \times N_{\text{RF}}$ matrix into a real vector via a linear operator

$$\text{vec}_{\text{H}} : \mathbb{C}^{N_{\text{RF}} \times N_{\text{RF}}} \rightarrow \mathbb{R}^L, \quad L \triangleq N_{\text{RF}}^2,$$

such that $\text{vec}_H(\mathbf{R})$ stacks $\Re\{\mathbf{R}\}$ and $\Im\{\mathbf{R}\}$ in a fixed order. Since (9) is a least-squares fit of a linear parametric covariance model, there exists a real matrix $\mathbf{C} \in \mathbb{R}^{L \times (d+1)}$ and a vector $\mathbf{y} \in \mathbb{R}^L$ such that

$$\text{vec}_H(\mathbf{R}_{\mathcal{M}}(\mathbf{p}, N_0)) = \mathbf{C}\mathbf{x}, \quad \text{vec}_H(\hat{\mathbf{R}}_{\text{FBA}}) = \mathbf{y}.$$

More explicitly, the k -th column of \mathbf{C} equals

$$\mathbf{c}_k = \text{vec}_H(\mathbf{a}_{\mathcal{M}}(\hat{\mu}_{k,\text{coarse}})\mathbf{a}_{\mathcal{M}}^H(\hat{\mu}_{k,\text{coarse}})), \quad k = 1, \dots, d,$$

and the last column corresponds to the noise contribution,

$$\mathbf{c}_{d+1} = \text{vec}_H(\mathbf{I}_{N_{\text{RF}}}).$$

The NNLS problem (9) can then be written as

$$\min_{\mathbf{x} \geq \mathbf{0}} \|\mathbf{y} - \mathbf{C}\mathbf{x}\|_2^2 = \min_{\mathbf{x} \geq \mathbf{0}} (\mathbf{y} - \mathbf{C}\mathbf{x})^\top (\mathbf{y} - \mathbf{C}\mathbf{x}).$$

Expanding the square and discarding the constant term $\mathbf{y}^\top \mathbf{y}$ yields the standard real-valued QP

$$\min_{\mathbf{x} \geq \mathbf{0}} \frac{1}{2} \mathbf{x}^\top \mathbf{H}_{\text{pow}} \mathbf{x} - \mathbf{q}_{\text{pow}}^\top \mathbf{x}, \quad (18)$$

with

$$\mathbf{H}_{\text{pow}} \triangleq 2\mathbf{C}^\top \mathbf{C}, \quad \mathbf{q}_{\text{pow}} \triangleq 2\mathbf{C}^\top \mathbf{y}.$$

The non-negativity constraints $\mathbf{x} \geq \mathbf{0}$ encode $\mathbf{p} \geq \mathbf{0}$ and $N_0 \geq 0$. In our implementation we add a small diagonal ridge εI to \mathbf{H}_{pow} (with $\varepsilon > 0$) for numerical stability before calling a standard NNLS/QP solver.

A.2 Toeplitz-PSD Covariance Projection

We now detail the Toeplitz-PSD projection problem (10). Let

$$\hat{\mathbf{R}}_s = \mathbf{A}(\hat{\mu}_{\text{coarse}}) \text{diag}(\hat{\mathbf{p}}_{\text{coarse}}) \mathbf{A}^H(\hat{\mu}_{\text{coarse}}) \in \mathbb{C}^{M \times M}$$

be the model-based full-aperture signal covariance obtained from the coarse power estimates. We consider the set \mathcal{T}^+ of Hermitian Toeplitz PSD matrices of dimension M .

Any Hermitian Toeplitz matrix $\mathbf{R} \in \mathcal{T}^+$ is fully specified by its first column

$$\mathbf{t} \triangleq [t_0, t_1, \dots, t_{M-1}]^\top \in \mathbb{C}^M,$$

with $t_0 \in \mathbb{R}$ and $t_\ell = r_\ell + js_\ell$ for $\ell \geq 1$. We parameterize \mathbf{R} by the real vector

$$\mathbf{z} \triangleq [t_0, r_1, \dots, r_{M-1}, s_1, \dots, s_{M-1}]^\top \in \mathbb{R}^{2M-1}.$$

There exists a fixed real matrix $\mathbf{T} \in \mathbb{R}^{L \times (2M-1)}$, with $L = M^2$, such that

$$\text{vec}_H(\mathbf{R}) = \mathbf{T}\mathbf{z},$$

where $\text{vec}_H(\cdot)$ is the Hermitian vectorization operator used in Appendix A. Likewise, define

$$\mathbf{y}_s \triangleq \text{vec}_H(\hat{\mathbf{R}}_s) \in \mathbb{R}^L.$$

The Frobenius-norm objective in (10) becomes

$$\|\mathbf{R} - \hat{\mathbf{R}}_s\|_F^2 = \|\text{vec}_H(\mathbf{R}) - \text{vec}_H(\hat{\mathbf{R}}_s)\|_2^2 = \|\mathbf{T}\mathbf{z} - \mathbf{y}_s\|_2^2.$$

Thus, ignoring for the moment the PSD constraint, the unconstrained Toeplitz projection is the real LS problem

$$\min_{\mathbf{z} \in \mathbb{R}^{2M-1}} \|\mathbf{T}\mathbf{z} - \mathbf{y}_s\|_2^2,$$

which can be written as the QP

$$\min_{\mathbf{z}} \frac{1}{2} \mathbf{z}^\top \mathbf{H}_{\text{toeplitz}} \mathbf{z} - \mathbf{q}_{\text{toeplitz}}^\top \mathbf{z}, \quad (19)$$

with

$$\mathbf{H}_{\text{toeplitz}} \triangleq 2\mathbf{T}^\top \mathbf{T}, \quad \mathbf{q}_{\text{toeplitz}} \triangleq 2\mathbf{T}^\top \mathbf{y}_s.$$

To enforce PSD, one can parameterize the Toeplitz covariance by its (oversampled) power spectral density. Specifically, for a dense grid of frequencies $\{\omega_m\}_{m=1}^{M_{\text{grid}}}$ on $[-\pi, \pi)$ we define

$$\lambda(\omega_m) = \sum_{\ell=-(M-1)}^{M-1} r_\ell e^{-j\ell\omega_m}, \quad m = 1, \dots, M_{\text{grid}},$$

where $r_{-\ell} = r_\ell^*$. The PSD constraint $\mathbf{R} \succeq \mathbf{0}$ is conservatively enforced by requiring

$$\lambda(\omega_m) \geq 0 \quad \text{for all } m,$$

which translates into a set of linear inequalities of the form

$$\mathbf{A}_{\text{psd}} \mathbf{z} \geq \mathbf{0}.$$

In summary, the Toeplitz–PSD projection (10) is implemented as the real-valued QP

$$\min_{\mathbf{z}} \frac{1}{2} \mathbf{z}^\top \mathbf{H}_{\text{toeplitz}} \mathbf{z} - \mathbf{q}_{\text{toeplitz}}^\top \mathbf{z} \quad \text{s.t.} \quad \mathbf{A}_{\text{psd}} \mathbf{z} \geq \mathbf{0}, \quad (20)$$

followed by reconstructing $\tilde{\mathbf{R}}_s$ from the optimal Toeplitz parameters \mathbf{z}^* . In practice we choose M_{grid} moderately larger than M (e.g., $M_{\text{grid}} = 4M$) and add a small ridge to $\mathbf{H}_{\text{toeplitz}}$ for numerical robustness.

B Covariance-Guided DFT Beam Selection Algorithm

This appendix provides pseudocode for the covariance-guided DFT beam selection procedure described in Section 3.3. The algorithm operates on the denoised full-aperture signal covariance $\tilde{\mathbf{R}}_s$ and sector-wise beam pools and returns, for each sector, a contiguous set of beams that maximizes the score defined in (11).

Algorithm 1 Covariance-Guided DFT Beam Selection

Require: $\tilde{\mathbf{R}}_s \in \mathbb{C}^{M \times M}$ (Hermitian PSD), sector-wise beam pools $\{\mathcal{B}_g\}_{g=1}^G$ with $\mathcal{B}_g \subset \{1, \dots, M\}$, beam-budget vector $\mathbf{K} = [K_1, \dots, K_G]^\top$ with $K_g \geq 2$, parameters $\gamma \geq 0$, $\alpha \geq 0$, optional pruning parameter $q \in \mathbb{N}$ (set $q = 0$ to disable pruning).

Ensure: Selected contiguous beam sets $\mathcal{S}_g^* \subset \mathcal{B}_g$ for $g = 1, \dots, G$.

- 1: Precompute the phase-shifted DFT beamforming matrix $\mathbf{B} = [\mathbf{b}_1, \dots, \mathbf{b}_M] \in \mathbb{C}^{M \times M}$, with $\mathbf{b}_m \in \mathbb{C}^M$ for $m = 1, \dots, M$.
- 2: Compute the beamspace covariance $\mathbf{R}_b = \mathbf{B}^H \tilde{\mathbf{R}}_s \mathbf{B}$ and per-beam energies $\rho_m = [\mathbf{R}_b]_{mm}$ for $m = 1, \dots, M$.
- 3: **for** $g = 1$ to G **do**
- 4: Let $\mathcal{B}_g = \{\kappa_1, \dots, \kappa_{L_g}\}$ be the sorted beam indices in sector g .
- 5: Set K_g from \mathbf{K} and clip it to $2 \leq K_g \leq L_g$.
- 6: Define the set of starting positions of a contiguous K_g -beam window: $\mathcal{S}_{\text{start}} \leftarrow \{1, \dots, L_g - K_g + 1\}$.
- 7: **if** $q > 0$ **and** $L_g > K_g$ **then**
- 8: Identify the q beams in \mathcal{B}_g with largest energy ρ_m and collect their positions (within $\{1, \dots, L_g\}$) in a set \mathcal{C}_{top} .
- 9: Let $h \leftarrow (K_g - 1)/2$ (assuming odd K_g ; for even K_g use $\lceil (K_g - 1)/2 \rceil$).
- 10: Prune the starting positions: $\mathcal{S}_{\text{start}} \leftarrow \{s \in \mathcal{S}_{\text{start}} : s + h \in \mathcal{C}_{\text{top}}\}$.
- 11: **end if**
- 12: Initialize best score $\text{score}^* \leftarrow -\infty$ and empty best set \mathcal{S}_g^* .
- 13: **for each** $s \in \mathcal{S}_{\text{start}}$ **do**
- 14: Define the candidate contiguous set $\mathcal{S}_g(s) \leftarrow \{\kappa_s, \kappa_{s+1}, \dots, \kappa_{s+K_g-1}\} \subset \mathcal{B}_g$.
- 15: Form the beam matrix $\mathbf{B}_g \leftarrow [\mathbf{b}_m]_{m \in \mathcal{S}_g(s)} \in \mathbb{C}^{M \times K_g}$.
- 16: Compute the Gram matrix $\mathbf{G}_g \leftarrow \mathbf{B}_g^H \mathbf{B}_g$ and projected covariance $\mathbf{C}_g \leftarrow \mathbf{B}_g^H \tilde{\mathbf{R}}_s \mathbf{B}_g$.
- 17: Regularize the Gram matrix: $\mathbf{G}_g^{(\gamma)} \leftarrow \mathbf{G}_g + \gamma \mathbf{I}_{K_g}$.
- 18: Compute the covariance-capture term $\text{cap} \leftarrow \text{tr}[(\mathbf{G}_g^{(\gamma)})^{-1} \mathbf{C}_g]$.
- 19: Compute the squared condition number $\kappa_g^2 \leftarrow \text{cond}(\mathbf{G}_g)^2$ (skip this window if \mathbf{G}_g is numerically singular).
- 20: Form the final score $\text{score} \leftarrow \text{cap}/(1 + \alpha \kappa_g^2)$.
- 21: **if** $\text{score} > \text{score}^*$ **then**
- 22: $\text{score}^* \leftarrow \text{score}$, $\mathcal{S}_g^* \leftarrow \mathcal{S}_g(s)$.
- 23: **end if**
- 24: **end for**
- 25: **end for**
- 26: **return** $\{\mathcal{S}_g^*\}_{g=1}^G$.

References

- [1] Samsung Research, “6G: The Next Hyper-Connected Experience for All,” [Online]. Available: https://cdn.codeground.org/nsr/downloads/researchareas/20201201_6G_Vision_web.pdf, 2020.
- [2] Q. Xue, C. Ji, S. Ma, J. Guo, Y. Xu, Q. Chen, and W. Zhang, “A Survey of Beam Management for mmWave and THz Communications Towards 6G,” *IEEE Communications Surveys & Tutorials*, vol. 26, no. 3, pp. 1520–1559, 2024.
- [3] A. F. Molisch, V. V. Ratnam, S. Han, Z. Li, S. L. H. Nguyen, L. Li, and K. Haneda, “Hybrid Beamforming for Massive MIMO: A Survey,” *IEEE Communications Magazine*, vol. 55, no. 9, pp. 134–141, 2017.
- [4] M. Cui and L. Dai, “Near-field wideband channel estimation for extremely large-scale MIMO,” *Science China Information Sciences*, vol. 66, no. 7, p. 172303, 2023.
- [5] M. R. Castellanos, S. Yang, C.-B. Chae, and R. W. Heath, “Embracing Reconfigurable Antennas in the Tri-hybrid MIMO Architecture for 6G and Beyond,” *IEEE Transactions on Communications*, pp. 1–1, 2025.
- [6] B. Shi, X. Jiang, N. Chen, Y. Teng, J. Lu, F. Shu, J. Zou, J. Li, and J. Wang, “Fast ambiguous DOA elimination method of DOA measurement for hybrid massive MIMO receiver,” *Science China Information Sciences*, vol. 65, no. 5, p. 159302, 2022.
- [7] A. Abdelbadie, M. Mostafa, S. Bameri, R. H. Gohary, and D. Thomas, “DoA Estimation for Hybrid Receivers: Full Spatial Coverage and Successive Refinement,” *IEEE Transactions on Signal Processing*, vol. 72, pp. 4730–4744, 2024.
- [8] Z. Zhuang, L. Xu, J. Li, J. Hu, L. Sun, F. Shu, and J. Wang, “Machine-learning-based high-resolution DOA measurement and robust directional modulation for hybrid analog-digital massive MIMO transceiver,” *Science China Information Sciences*, vol. 63, no. 8, p. 180302, Jul 2020.
- [9] K. Xu, X. Xia, C. Li, W. Xie, J. Liu, R. Zhu, and H. He, “Robust DOA estimation and tracking for integrated sensing and communication massive MIMO OFDM systems,” *Science China Information Sciences*, vol. 66, no. 10, p. 202302, 2023.
- [10] Y. Huang, Z. Zhang, J. Che, Z. Yang, Q. Yang, and K.-K. Wong, “Self-attention reinforcement learning for multi-beam combining in mmWave 3D-MIMO systems,” *Science China Information Sciences*, vol. 66, no. 6, p. 162304, 2023.
- [11] S. Li, Y. Liu, L. You, W. Wang, H. Duan, and X. Li, “Covariance Matrix Reconstruction for DOA Estimation in Hybrid Massive MIMO Systems,” *IEEE Wireless Communications Letters*, vol. 9, no. 8, pp. 1196–1200, 2020.
- [12] Z. Yang, J. Li, P. Stoica, and L. Xie, 2018, chapter 11, “Sparse methods for direction-of-arrival estimation”, in *Academic Press Library in Signal Processing, Volume 7*, edited by R. Chellappa and S. Theodoridis, Academic Press, pp. 509–581.
- [13] Y. Huang, Y. Zhang, J. Tao, C. Wen, G. Liao, and W. Hong, “Off-grid DOA estimation via a deep learning framework,” *Science China Information Sciences*, vol. 66, no. 12, p. 222305, 2023.
- [14] R. R. Pote and B. D. Rao, “Maximum Likelihood-Based Gridless DoA Estimation Using Structured Covariance Matrix Recovery and SBL With Grid Refinement,” *IEEE Transactions on Signal Processing*, vol. 71, pp. 802–815, 2023.

- [15] C. F. Mecklenbräuker, P. Gerstoft, E. Ollila, and Y. Park, “Robust and sparse M-estimation of DOA,” *Signal Processing*, vol. 220, p. 109461, 2024.
- [16] Y. Park, P. Gerstoft, and C. F. Mecklenbräuker, “Atom-Constrained Gridless DOA Refinement With Wirtinger Gradients,” *IEEE Open Journal of Signal Processing*, vol. 5, pp. 1134–1146, 2024.
- [17] T. Liu, F. Matter, A. Sorg, M. E. Pfetsch, M. Haardt, and M. Pesavento, “Joint Sparse Estimation with Cardinality Constraint via Mixed-Integer Semidefinite Programming,” in *IEEE 9th International Workshop on CAMSAP*, 2023, pp. 106–110.
- [18] J. Zhang, D. Rakhimov, and M. Haardt, “Gridless Channel Estimation for Hybrid mmWave MIMO Systems via Tensor-ESPRIT Algorithms in DFT Beamspace,” *IEEE Journal of Selected Topics in Signal Processing*, vol. 15, no. 3, pp. 816–831, 2021.
- [19] D. Rakhimov and M. Haardt, “Analytical Performance Assessment of 1-D ESPRIT in DFT Beamspace in Terms of Physical Parameters,” in *2023 57th Asilomar Conference on Signals, Systems, and Computers*, 2023, pp. 1264–1270.
- [20] —, “Equivalence of Aperture Reduction in Element Space and Constrained Combination of DFT Beams in Beamspace,” in *IEEE ICASSP*, 2023, pp. 1–5.
- [21] S. Shahsavari, P. Sarangi, and P. Pal, “Beamspace ESPRIT for mmWave Channel Sensing: Performance Analysis and Beamformer Design,” *Frontiers in Signal Processing*, vol. Volume 1 - 2021, 2022.
- [22] H. L. V. Trees, *Optimum Array Processing*. John Wiley & Sons, 2002, Chap. 8, “Parameter Estimation I: Maximum Likelihood”, pp. 917–1138.